Dynamic simulation of flexible fibers composed of linked rigid bodies

Russell F. Ross
Department of Engineering Mechanics and Astronautics, University of Wisconsin–Madison, Madison, Wisconsin 53706

Daniel J. Klingenberg
Department of Chemical Engineering and Rheology Research Center, University of Wisconsin–Madison, Madison, Wisconsin 53706

(Received 28 May 1996; accepted 10 September 1996)

A particle-level simulation method is employed to study the dynamics of flowing suspensions of rigid and flexible fibers. Fibers are modeled as chains of prolate spheroids connected through ball and socket joints. By varying the resistance in the joints, both flexible and rigid fibers can be modeled. Repulsive interactions between fibers are included, but hydrodynamic interactions and particle inertia are neglected in this implementation. The motion of a fiber is determined by solving the translational and rotational equations of motion for each spheroid. Simulations of isolated fibers in shear flow demonstrate that the method can reproduce known dynamical behavior of both rigid and flexible fibers. The transient behavior in the suspension relative viscosity under simple shear flow was also investigated. An oscillatory response similar to the experimental observations of Ivanov *et al.* was obtained for rigid fibers. Fiber flexibility reduced the period of oscillation, but had little effect on steady-state viscosities. These results verify that rigid and flexible fibers can be modeled with linked rigid prolate spheroids. Modeling fibers with fewer elongated bodies, as opposed to many spheres, significantly reduces computation time and facilitates the study of suspensions of many interacting, long fibers. © *1997 American Institute of Physics.* [S0021-9606(97)50747-6]

I. INTRODUCTION

When a suspension of fibers is subjected to a flow field, the fibers rotate, translate, and deform. The resulting changes in the suspension microstructure can have dramatic effects on the material's macroscopic properties. In fiber-reinforced composites, changes in fiber orientation and spatial distribution affect such material properties as thermal expansivity, elastic modulus, and thermal and electrical conductivity.[1] In wood pulp suspensions, a nonuniform microstructure impacts such papermaking processes as screening and cleaning, refining, and sheet formation. The nonuniformities are attributed to the tendency of wood pulp fibers to entangle with each other forming small, concentrated domains called flocs. The purpose of this paper is to introduce a molecular dynamics-like simulation method that can be used to investigate the microstructure and rheology of fiber suspensions and their dependence on relevant suspension parameters.

Much of our current understanding of the behavior of flowing fiber suspensions has come from the work of Jeffery[2] and Forgacs and Mason.[3,4] Jeffery modeled a fiber as a rigid ellipsoid, and determined that an isolated fiber in simple shear flow rotates in a periodic orbit while the center of mass translates affinely with the bulk flow. The period is a function of aspect ratio and shear rate and the orbit depends on the initial orientation of the ellipsoid relative to the shear plane. Forgacs and Mason, who examined fiber motion in a Couette device, observed that a fiber can undergo a variety of complex rotational motions depending on its flexibility. For example, a fiber could bend into an S-shape or coil up as it rotated, depending on its flexibility, aspect ratio, and the shear rate. These results demonstrate the sensitivity of suspension structure to aspect ratio, hydrodynamic forces, and fiber flexibility, and identify characteristic fiber motions in flow fields.

In a suspension containing many fibers, interactions between fibers perturb the motions described above. Such interactions may arise from hydrodynamic or colloidal forces, excluded volume (short-range repulsion), or friction. Such a complicated system of many interacting, flexible bodies precludes a simple method to relate fiber properties and interactions to suspension structure and rheology. Studies have thus understandably employed approximations to real systems in order to formulate more tractable models.

Numerous studies have focused on suspensions of rigid elongated bodies. Starting with Batchelor's[5] ''cell model'' for rigid fiber suspensions, Dinh and Armstrong,[6] Toll and Månson,[7] and Rahnama *et al.*[8] incorporated random fiber orientations, friction between fibers, and hydrodynamic interactions, respectively, into structural theories. Folgar and Tucker[9] added a rotary diffusion term to Jeffery's equations to represent the influence of mechanical and hydrodynamic interactions on structure evolution. Claeys and Brady[10–12] employ a particle-level simulation method, which accurately accounts for hydrodynamic interactions, to examine suspensions of rigid prolate spheroids. Yamane *et al.*[13] simulate the dynamics of rigid cylinders, including a lubrication approximation to hydrodynamic interactions.

Flexible fibers have been treated as chains of rigid bodies. Yamamoto and Matsuoka[14–17] have developed a method for simulating such fibers in shear flow. The fiber is modeled as a chain of osculating rigid spheres connected through

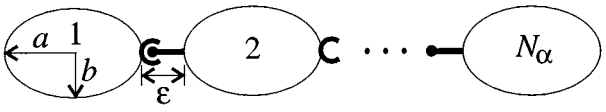

FIG. 1. Linked rigid body model for a flexible fiber. a and b are the spheroid major and minor axis lengths, respectively. The parameter ϵ is the separation between spheroids (usually $\epsilon = 0.01b$).

springs, with additional potentials to mimic resistance to bending and twisting. Chain connectivity is maintained by constraints, producing equations that must be solved iteratively and simultaneously with the equations of motion. This method has been used to investigate the dynamics of isolated fibers,[14] the single fiber contribution to the suspension viscosity,[15] flow-induced fiber fracture of isolated fibers,[16] and fiber suspension behavior.[17]

In this paper, we present a particle-level simulation method for the structural evolution of flexible fiber suspensions in shear flow. The fiber model is similar to that used by Yamamoto and Matsuoka,[14] except that we employ a chain of rigid prolate spheroids connected through ball and socket joints. This model eliminates the need for iterative constraints to maintain fiber connectivity, and can represent large-aspect ratio fibers with relatively few bodies. These features help to reduce computations, facilitating simulation of concentrated suspensions.

The fiber model and simulation method are described in Section II. The fiber connectivity, kinematics, and dynamics are presented in Sections II A, II B, and II C, respectively. The formalism follows that described by Wittenburg[18] for systems of linked rigid bodies, which has also been implemented in a model for polymer dynamics.[19] Simulation results for single fiber dynamics are presented in Section III. Here we show that the method reproduces salient features of the dynamics of rigid and flexible fibers in simple shear flow. In Section IV, simulation results for rheological properties are presented. We highlight the dependence of the suspension viscosity and transient effects on the shear rate and fiber flexibility. Rheological properties will be examined in more detail in a future publication.

II. FIBER MODEL AND SIMULATION METHOD

Each fiber α in a suspension of flexible fibers is represented by N_α rigid prolate spheroids (each with aspect ratio a/b) connected through $N_\alpha - 1$ ball and socket joints (see Fig. 1). The three degrees of rotational freedom in each joint enable the model to bend and twist much like a real fiber. To mimic fiber elastic properties, resistance potentials are defined in the joints (these are described in Section II C). Fiber extensibility is neglected since it is typically small compared to other forms of deformation. Extensibility, as well as ''hooks'' and ''bends,''[20] can be incorporated via modified ball and socket joints. The motion of the continuous phase molecules is not considered explicitly—the suspending fluid only influences fiber dynamics via hydrodynamic resistance and buoyancy.

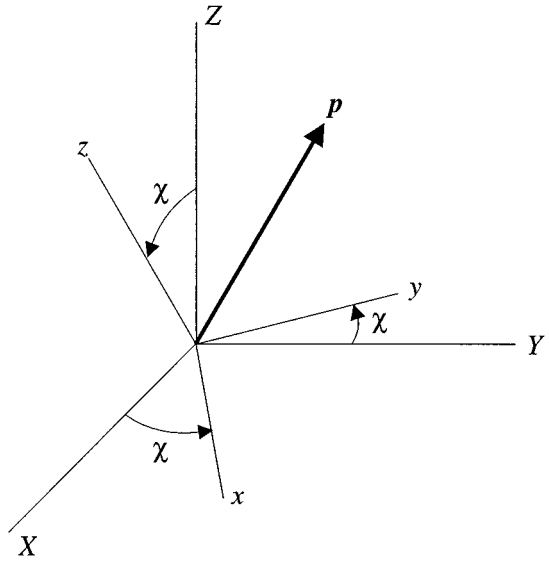

FIG. 2. Illustration of Euler's theorem for the orientation of a rigid body. X-Y-Z is the reference frame and x-y-z is the body-fixed frame.

The centers of mass of the spheroids in fiber α are defined by the Cartesian vectors $\mathbf{r}_i^\alpha (i = 1, \ldots, N_\alpha)$, measured from a fixed reference frame. The orientations are defined in terms of the Euler parameters q_{1i}^α, q_{2i}^α, q_{3i}^α, and q_{4i}^α $(i = 1, \ldots, N_\alpha)$. Euler parameters are a set of generalized orientation coordinates derived from Euler's theorem.[21] This theorem states that any orientation of the x-y-z body-fixed frame can be achieved by a rotation χ from the X-Y-Z reference frame about some unit vector $\mathbf{p}$, as shown in Fig. 2. Definitions of the parameters follow as

$$q_1 = \cos\frac{\chi}{2}, \quad q_2 = p_x \sin\frac{\chi}{2},$$
$$q_3 = p_y \sin\frac{\chi}{2}, \quad q_4 = p_z \sin\frac{\chi}{2}, \tag{1}$$

where the vector $\mathbf{p}$ is referenced to the body-fixed frame. In the model, the Euler parameters are defined such that q_{11}^α, q_{21}^α, q_{31}^α, and q_{41}^α orient spheroid 1 in the fixed reference frame, and q_{1i}^α, q_{2i}^α, q_{3i}^α, and q_{4i}^α $(i = 2, \ldots, N_\alpha)$ orient spheroid i relative to a body-fixed reference frame at the center of mass of spheroid $i-1$. The body-fixed reference frames are orientated such that the x-axis is along the major spheroidal axis pointing toward the larger numbered body. Euler parameters are used because they do not possess numerical singularities, and the components of the transformation matrix between reference frames of contiguous bodies [see Eqs. (13) and (14) below] are only quadratic functions of the parameters.

We now focus on the development of the dynamical equations. The approach follows a formalism by Wittenburg for systems of linked rigid bodies.[18] In Section II A, system connectivity is discussed, which is required to specify fiber kinematics. The kinematics are then described in Section

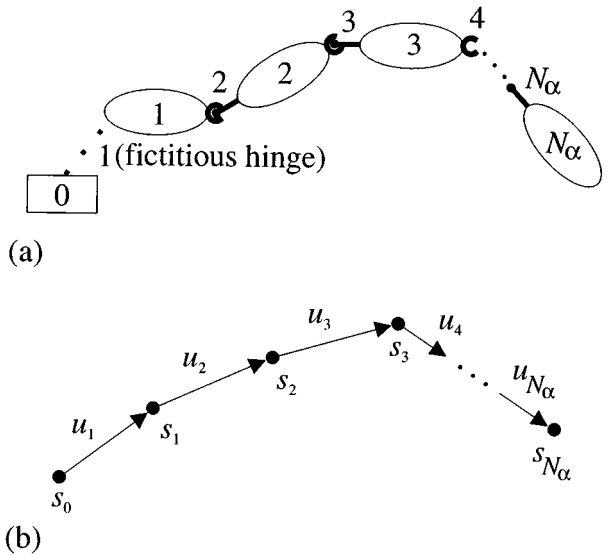

FIG. 3. (a) Illustration of body and hinge index numbering used in constructing the connectivity matrices, (b) system graph for (a).

II B. Finally, fiber dynamics, governed by Newton's second law and the law of moment of momentum, are described in Section II C.

A. System connectivity

Connectivity matrices are employed to describe how the bodies (spheroids) and joints (hinges) are connected to one another. The matrices are constructed by first numbering the bodies and joints. Body 0 is reserved for the fixed reference frame and joint 1 is between body 0 and body 1. Body 1 is designated as an end body in the model. Since the fiber is not coupled to an external body in the fixed reference frame, joint 1 is fictitious but is included in the analysis only to obtain square matrices. The other bodies and joints are numbered in increasing order continuing from body 1 (see Fig. 3). This index information is then converted into a system graph, which consists of points, called vertices, and lines connecting the vertices, called arcs. The vertices $(s_1,\ldots,s_{N_\alpha})$ represent the bodies and the arcs $(u_1,\ldots,u_{N_\alpha})$ represent the joints. The direction of an arc is from a smaller to a larger numbered body.

From the system graph, two integer functions, $i^{(+)\alpha}(a)$ and $i^{(-)\alpha}(a)$, are defined to establish relationships between arc indices and vertex indices. For arc number $a=1,\ldots,N_\alpha$, $i^{(+)\alpha}(a)$ is the index of the vertex from which arc u_a emanates, and $i^{(-)\alpha}(a)$ is the index of the vertex toward which arc u_a is pointing. These integer functions are given in Table I for the system graph depicted in Fig. 3. Connectivity matrices $\underline{S}^\alpha$ and $\underline{T}^\alpha$ are defined in terms of the integer functions and the system graph,

$$S^\alpha_{ia}=\begin{cases}+1 & \text{if } i=i^{(+)\alpha}(a)\\ -1 & \text{if } i=i^{(-)\alpha}(a),\quad i,a=1,\ldots,N_\alpha\\ 0 & \text{otherwise,}\end{cases}\tag{2}$$

and

$$T^\alpha_{ai}=\begin{cases}+1 & \text{if } u_a \text{ belongs to the path between } s_0 \text{ and } s_i\\ & \text{and is directed toward } s_0,\\ -1 & \text{if } u_a \text{ belongs to the path between } s_0 \text{ and } s_i\\ & \text{and is directed away from } s_0,\\ 0 & \text{if } u_a \text{ does not belong to the path between}\\ & s_0 \text{ and } s_i,\\ & i,a=1,\ldots,N_\alpha.\end{cases}\tag{3}$$

For the numbering scheme presented in Fig. 3, these matrices are

$$\underline{S}^\alpha=\begin{bmatrix}-1 & 1 & 0 & \cdots & 0\\ 0 & -1 & 1 & \ddots & \vdots\\ & & \ddots & \ddots & 0\\ \vdots & & \ddots & -1 & 1\\ 0 & & \cdots & 0 & -1\end{bmatrix},$$

$$\underline{T}^\alpha=\begin{bmatrix}-1 & -1 & -1 & \cdots & -1\\ 0 & -1 & -1 & \cdots & -1\\ & & -1 & \cdots & -1\\ \vdots & & \ddots & \ddots & \vdots\\ 0 & & \cdots & 0 & -1\end{bmatrix}.$$

These matrices possess the property

$$\underline{T}^\alpha\underline{S}^\alpha=\underline{S}^\alpha\underline{T}^\alpha=\underline{E}^\alpha,\tag{4}$$

where $\underline{E}^\alpha$ is an $N_\alpha\times N_\alpha$ identity matrix.

TABLE I. Integer functions $i^{(+)\alpha}(a)$ and $i^{(-)\alpha}(a)$ for the system graph depicted in Fig. 3.

a	1	2	3	4	5	$\cdots$	N_α
$i^{(+)\alpha}(a)$	0	1	2	3	4	$\cdots$	$N_\alpha-1$
$i^{(-)\alpha}(a)$	1	2	3	4	5	$\cdots$	N_α

B. Kinematics

A set of body-fixed connectivity vectors, $\mathbf{c}^\alpha_{ia}$ $(i,a=1,\ldots,N_\alpha)$, are introduced to establish the relationship between the spheroid positions. These vectors extend from the center of mass of spheroid i to joint a (see Fig. 4). For a joint a not connected with spheroid i, this vector is defined as $\mathbf{0}$. These vectors are related to the spheroid positions by

$$(\mathbf{r}^\alpha_{i^{(-)\alpha}(a)}+\mathbf{c}^\alpha_{i^{(-)\alpha}(a)a})-(\mathbf{r}^\alpha_{i^{(+)\alpha}(a)}+\mathbf{c}^\alpha_{i^{(+)\alpha}(a)a})=0,\quad a=1,\ldots,N_\alpha.\tag{5}$$

These equations can be combined into a single matrix equation using the connectivity matrix $\underline{S}^\alpha$,

$$(\underline{S}^\alpha)^\dagger\underline{\mathbf{r}}^\alpha+(\underline{\mathbf{C}}^\alpha)^\dagger\underline{1}_{N_\alpha}=0,\tag{6}$$

where $\underline{\mathbf{r}}^\alpha=[\mathbf{r}^\alpha_1\cdots\mathbf{r}^\alpha_{N_\alpha}]^\dagger$, $\underline{1}_{N_\alpha}$ is an $N_\alpha\times 1$ matrix of ones, and $\underline{\mathbf{C}}^\alpha$ is an $N_\alpha\times N_\alpha$ matrix with components $\mathbf{C}^\alpha_{ia}=S^\alpha_{ia}\mathbf{c}^\alpha_{ia}$

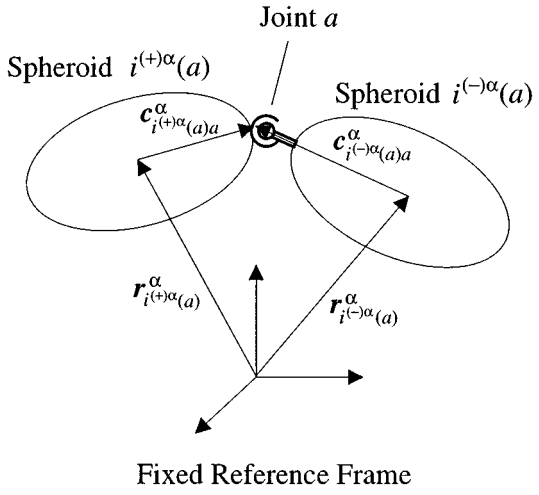

(a)

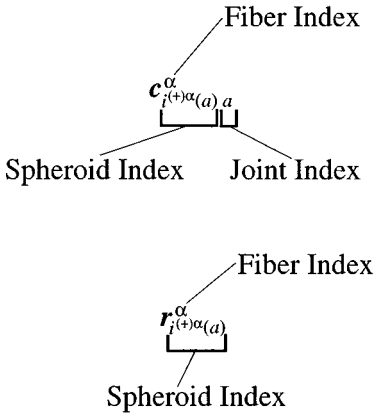

(b)

FIG. 4. (a) Illustration of the connectivity vectors used in the model kinematics, and (b) the notation used with the connectivity and position vectors.

(the superscript † denotes transpose). Multiplying Eq. (6) by $(\underline{T}^{\alpha})^{\dagger}$ and using the identity given in Eq. (4), the spheroid positions may be expressed in terms of the connectivity vectors,

$$\underline{\mathbf{r}}^{\alpha}=-(\underline{\mathbf{C}}^{\alpha}\underline{T}^{\alpha})^{\dagger}\underline{1}_{N_{\alpha}} \quad \text{or} \quad \mathbf{r}_i^{\alpha}=\sum_{j=1}^{N_{\alpha}}\mathbf{d}_{ji}^{\alpha}, \tag{7}$$

where $\mathbf{d}_{ji}^{\alpha}=-(\underline{\mathbf{C}}^{\alpha}\underline{T}^{\alpha})_{ji}$.

It is convenient to change the reference body in Eq. (7) from an external body hinged to spheroid 1 to the fiber center of mass. This transformation is performed using

$$\mathbf{r}_i^{\alpha}=\mathbf{R}_i^{\alpha}+\mathbf{r}_C^{\alpha}, \tag{8}$$

where $\mathbf{R}_i^{\alpha}$ is the center of mass of spheroid i relative to the fiber center of mass, and $\mathbf{r}_C^{\alpha}$ is the center of mass of fiber α in the fixed reference frame. Substituting Eq. (7) into Eq. (8) and multiplying by the $(N_{\alpha}\times N_{\alpha})$ matrix $\underline{\nu}^{\alpha}$ $(\nu_{ij}^{\alpha}=\delta_{ij}-1/N_{\alpha})$ the spheroid positions relative to the fiber center of mass are

$$\underline{\mathbf{R}}^{\alpha}=-(\underline{\mathbf{C}}^{\alpha}\underline{T}^{\alpha}\underline{\nu}^{\alpha})^{\dagger}\underline{1}_{N_{\alpha}} \quad \text{or} \quad \mathbf{R}_i^{\alpha}=\sum_{j=1}^{N_{\alpha}}\mathbf{b}_{ji}^{\alpha}, \tag{9}$$

where $\mathbf{b}_{ji}^{\alpha}=-(\underline{\mathbf{C}}^{\alpha}\underline{T}^{\alpha}\underline{\nu}^{\alpha})_{ji}$. Inserting Eq. (9) into Eq. (8),

$$\mathbf{r}_i^{\alpha}=\sum_{j=1}^{N_{\alpha}}\mathbf{b}_{ji}^{\alpha}+\mathbf{r}_C^{\alpha}. \tag{10}$$

Differentiating Eq. (10) with respect to time, the translational velocity of spheroid i is

$$\dot{\mathbf{r}}_i^{\alpha}=\sum_{j=1}^{N_{\alpha}}\boldsymbol{\omega}_j^{\alpha}\times\mathbf{b}_{ji}^{\alpha}+\dot{\mathbf{r}}_C^{\alpha}, \tag{11}$$

where $\boldsymbol{\omega}_j^{\alpha}$ is absolute angular velocity of spheroid j. The motion of the fiber center of mass, $\dot{\mathbf{r}}_C^{\alpha}$ is discussed later in connection with the dynamical equations.

The absolute angular velocity of spheroid i is related to the relative angular velocities of spheroids $i-1$ through the connectivity matrix $\underline{T}^{\alpha}$,

$$\boldsymbol{\omega}_i^{\alpha}=-\sum_{a=1}^{N_{\alpha}}T_{ai}^{\alpha}\boldsymbol{\Omega}_a^{\alpha}, \tag{12}$$

where $\boldsymbol{\Omega}_a^{\alpha}$ is the angular velocity of spheroid $i^{(-)\alpha}(a)$ relative to that of spheroid $i^{(+)\alpha}(a)$. The transformation between reference frames on contiguous spheroids, connected through joint a, is described by

$$\underline{\mathbf{e}}^{(i^{(+)\alpha}(a))}=G_a^{\alpha}\underline{\mathbf{e}}^{(i^{(-)\alpha}(a))}, \tag{13}$$

where $\underline{\mathbf{e}}^{(i^{(+)\alpha}(a))}$ and $\underline{\mathbf{e}}^{(i^{(-)\alpha}(a))}$ represent Cartesian base vectors of reference frames fixed at the centers of mass of spheroids $i^{(+)\alpha}(a)$ and $i^{(-)\alpha}(a)$, respectively. The orthogonal transformation matrix G_a^{α} is defined in terms of the Euler parameters,

$$G_a^{\alpha}=2\begin{bmatrix}(q_{a1}^{\alpha})^2+(q_{a2}^{\alpha})^2-\frac{1}{2} & q_{a2}^{\alpha}q_{a3}^{\alpha}-q_{a1}^{\alpha}q_{a4}^{\alpha} & q_{a2}^{\alpha}q_{a4}^{\alpha}+q_{a1}^{\alpha}q_{a3}^{\alpha}\\ q_{a2}^{\alpha}q_{a3}^{\alpha}+q_{a1}^{\alpha}q_{a4}^{\alpha} & (q_{a1}^{\alpha})^2+(q_{a3}^{\alpha})^2-\frac{1}{2} & q_{a3}^{\alpha}q_{a4}^{\alpha}-q_{a1}^{\alpha}q_{a2}^{\alpha}\\ q_{a2}^{\alpha}q_{a4}^{\alpha}-q_{a1}^{\alpha}q_{a3}^{\alpha} & q_{a3}^{\alpha}q_{a4}^{\alpha}+q_{a1}^{\alpha}q_{a2}^{\alpha} & (q_{a1}^{\alpha})^2+(q_{a4}^{\alpha})^2-\frac{1}{2}\end{bmatrix}. \tag{14}$$

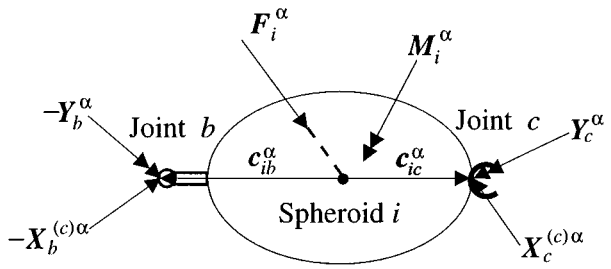

FIG. 5. Free-body diagram for spheroid i in fiber α.

C. Dynamics

The dynamical equations describing spheroid motion in a fiber are derived from Newton's law and the law of moment of momentum. To apply these laws, the spheroids are separated at the joints to produce N_α free-body diagrams. The free-body diagram for spheroid i is given in Fig. 5, where $\mathbf{F}_i^\alpha$ is the resultant external force acting through the center of mass, $\mathbf{M}_i^\alpha$ is the resultant external torque, $\mathbf{X}_b^{(c)\alpha}$ and $\mathbf{X}_c^{(c)\alpha}$ are the internal constraint forces in joints b and c respectively, and $\mathbf{Y}_b^\alpha$ and $\mathbf{Y}_c^\alpha$ are the resultant internal torques in joints b and c respectively. From the free-body diagram for spheroid i Newton's second law takes the form

$$m_i^\alpha \ddot{\mathbf{r}}_i^\alpha = \mathbf{F}_i^\alpha + \sum_{a=1}^{N_\alpha} S_{ia}^\alpha \mathbf{X}_a^{(c)\alpha}, \tag{15}$$

and the law of moment of momentum is

$$\dot{\mathbf{H}}_i^\alpha = \mathbf{M}_i^\alpha + \sum_{a=1}^{N_\alpha} S_{ia}^\alpha (\mathbf{c}_{ia}^\alpha \times \mathbf{X}_a^{(c)\alpha} + \mathbf{Y}_a^\alpha), \tag{16}$$

where m_i^α, $\ddot{\mathbf{r}}_i^\alpha$, and $\dot{\mathbf{H}}_i^\alpha$, represent the mass, translational acceleration, and time rate of change of angular momentum of spheroid i, respectively. The resultant external force is the combination of hydrodynamic forces $\mathbf{F}_i^{(h)\alpha}$, interparticle forces $\mathbf{F}_i^{(p)\alpha}$, and body forces $\mathbf{F}_i^{(g)\alpha}$, and the resultant external torque is the combination of hydrodynamic torques $\mathbf{M}_i^{(h)\alpha}$, and torques produced by external moments or interparticle forces $\mathbf{M}_i^{(p)\alpha}$.

If hydrodynamic interactions and fluid inertia are neglected, the hydrodynamic forces and torques acting on spheroid i suspended in a Newtonian fluid undergoing a linear flow characterized by the rate of strain tensor $\mathbf{E}^{(\infty)}$ and vorticity $\mathbf{\Omega}^{(\infty)}$ are[22]

$$\mathbf{F}_i^{(h)\alpha} = \mathbf{A}_i^{(h)\alpha} \cdot (\mathbf{U}_i^{(\infty)\alpha} - \dot{\mathbf{r}}_i^\alpha), \tag{17}$$

and

$$\mathbf{M}_i^{(h)\alpha} = \mathbf{C}_i^{(h)\alpha} \cdot (\mathbf{\Omega}^{(\infty)} - \boldsymbol{\omega}_i^\alpha) + \tilde{\mathbf{H}}_i^{(h)\alpha} : \mathbf{E}^{(\infty)}, \tag{18}$$

where $\mathbf{U}_i^{(\infty)\alpha}$ is the ambient fluid translational velocity evaluated at the center of mass of spheroid i. The resistance tensors $\mathbf{A}_i^{(h)\alpha}$, $\mathbf{C}_i^{(h)\alpha}$, and $\tilde{\mathbf{H}}_i^{(h)\alpha}$, which depend only on the instantaneous orientation of spheroid i, relate the force and torque exerted by the suspending fluid on spheroid i due to its translational and angular motion.

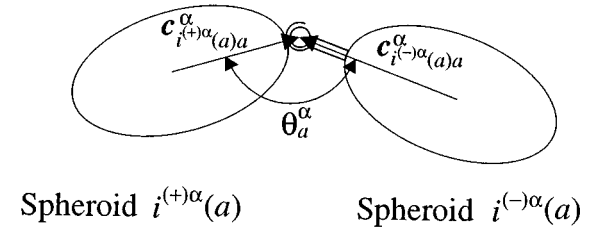

(a)

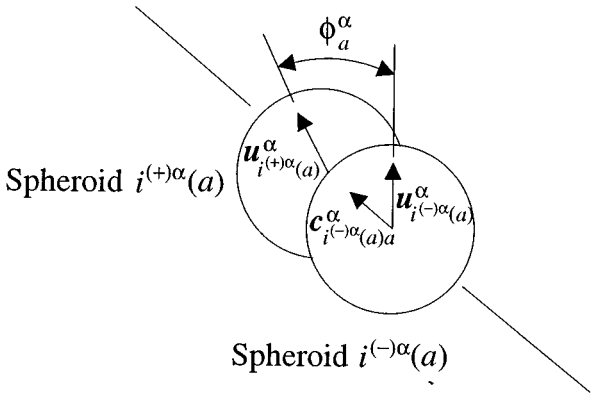

(b)

FIG. 6. (a) Definition of bending and (b) twisting angles used in the resistance torques.

The interparticle force $\mathbf{F}_i^{(p)\alpha}$ describes any inter- or intrafiber interactions, such as colloidal forces, short-range repulsion, and friction between fibers. Here we consider interparticle forces that depend only on the instantaneous spheroid positions and orientations. The torque $\mathbf{M}_i^{(p)\alpha}$ is used to include any externally applied moments or interparticle forces that do not act through the spheroid center of mass. The body force due to gravity is $\mathbf{F}_i^{(g)\alpha} = \frac{4}{3}\pi a b^2 \Delta\rho \mathbf{g}$, where $\mathbf{g}$ is the acceleration of gravity and $\Delta\rho$ is the density difference between a fiber and the suspending fluid.

The resultant internal torques in the joints, $\mathbf{Y}_a^\alpha$ $(a=2,\ldots,N_\alpha)$, incorporate resistance to bending and twisting into the fiber model, in order to mimic the elastic behavior of a real fiber. The bending and twisting torques are defined independently and superposed. The bending torque $\mathbf{Y}_a^{(B)\alpha}$ is defined in terms of the angle θ_a^α between the vectors $\mathbf{c}_{i^{(-)\alpha}(a)a}^\alpha$ and $\mathbf{c}_{i^{(+)\alpha}(a)a}^\alpha$ (see Fig. 6). The magnitude is assumed to be proportional to the difference between this angle and its equilibrium value, $\theta_a^{(0)\alpha}$ ($\theta_a^{(0)\alpha} = \pi$ for a straight fiber),

$$\mathbf{Y}_a^{(B)\alpha} = -k_B^\alpha (\theta_a^\alpha - \theta_a^{(0)\alpha}) \mathbf{n}_{pb}. \tag{19}$$

$\mathbf{n}_{pb}$ is the unit vector normal to the plane of bending,

$$\mathbf{n}_{pb} = \frac{\mathbf{c}_{i^{(-)\alpha}(a)a}^\alpha \times \mathbf{c}_{i^{(+)\alpha}(a)a}^\alpha}{\| \mathbf{c}_{i^{(-)\alpha}(a)a}^\alpha \times \mathbf{c}_{i^{(+)\alpha}(a)a}^\alpha \|}, \tag{20}$$

and θ_a^α is given by

$$\cos\theta_a^\alpha = \frac{\mathbf{c}^\alpha_{i^{(-)\alpha(a)a}} \cdot \mathbf{c}^\alpha_{i^{(+)\alpha(a)a}}}{\|\mathbf{c}^\alpha_{i^{(-)\alpha(a)a}}\| \|\mathbf{c}^\alpha_{i^{(+)\alpha(a)a}}\|}. \tag{21}$$

The bending constant k_B^α describes flexural rigidity of the fiber model. This quantity is related to the bending stiffness of an elastic cylinder (Young's modulus E and moment of inertia I) for small deformations via

$$k_B^\alpha = \frac{EI}{a}. \tag{22}$$

The twisting torque $\mathbf{Y}_a^{(T)\alpha}$ is defined in terms of the angle of twist ϕ_a^α between contiguous spheroids about an axis defined by the vector $\mathbf{c}^\alpha_{i^{(-)\alpha(a)a}}$ (see Fig. 6). The magnitude is assumed to be proportional to the difference between this angle and its equilibrium value, $\phi_a^{(0)\alpha}$ ($\phi_a^{(0)\alpha}=0$ for a nontwisted fiber),

$$\mathbf{Y}_a^{(T)\alpha} = -k_T^\alpha (\phi_a^\alpha - \phi_a^{(0)\alpha}) \frac{\mathbf{c}^\alpha_{i^{(-)\alpha(a)a}}}{\|\mathbf{c}^\alpha_{i^{(-)\alpha(a)a}}\|}. \tag{23}$$

To calculate ϕ_a^α body-fixed unit vectors $\mathbf{u}_i^\alpha$ are introduced. These vectors extend from the center of mass and are orientated perpendicular to the $\mathbf{c}_{ia}^\alpha$ vectors. The angle is then given by,

$$\cos\ \phi_a^\alpha = \frac{\mathbf{u}^\alpha_{i^{(-)\alpha(a)}} \cdot \mathbf{u}'_a}{\|\mathbf{u}'_a\|}, \tag{24}$$

where $\mathbf{u}'_a = \mathbf{u}^\alpha_{i^{(+)\alpha(a)}} - \mathbf{u}^\alpha_{i^{(+)\alpha(a)}} \cdot \mathbf{c}^\alpha_{i^{(-)\alpha(a)a}}$. The twisting constant k_T^α describes the torsional rigidity of the fiber model. This quantity is related to the torsional rigidity of an elastic cylinder (shear modulus G and polar moment of inertia J) for small deformations via

$$k_T^\alpha = \frac{GJ}{a}. \tag{25}$$

Nonuniform elastic properties or structural imperfections in a fiber may be modeled by allowing k_B^α and k_T^α to vary among the joints. The equilibrium angles $\theta_a^{(0)\alpha}$ may be altered to describe bent fibers.

Now that the system forces and torques have been defined, the final form of the dynamical equations can be developed. Neglecting particle inertia, Eqs. (15) and (16) reduce to

$$\mathbf{F}_i^{(h)\alpha} + \mathbf{F}_i^{(p)\alpha} + \mathbf{F}_i^{(g)\alpha} + \sum_{a=1}^{N_\alpha} S_{ia}^\alpha \mathbf{X}_a^{(c)\alpha} = 0, \tag{26}$$

and

$$\mathbf{M}_i^{(h)\alpha} + \mathbf{M}_i^{(p)\alpha} + \sum_{a=1}^{N_\alpha} S_{ia}^\alpha (\mathbf{c}_{ia}^\alpha \times \mathbf{X}_a^{(c)\alpha} + \mathbf{Y}_a^\alpha) = 0. \tag{27}$$

Inserting Eq. (11) into Eq. (17) and substituting the resulting expression into Eq. (26), the motion of the fiber center of mass is obtained by summing the translational equations of motion for $i=1$ to N_α,

$$\dot{\mathbf{r}}_C^\alpha = -(\mathbf{A}^\alpha)^{-1} \cdot \left[\sum_{j=1}^{N_\alpha} \sum_{k=1}^{N_\alpha} \mathbf{A}_j^{(h)\alpha} \cdot (\boldsymbol{\omega}_k^\alpha \times \mathbf{b}_{kj}^\alpha) - \sum_{j=1}^{N_\alpha} (\mathbf{A}_j^{(h)\alpha} \cdot \mathbf{U}_j^{(\infty)\alpha} + \mathbf{F}_j^{(p)\alpha} + \mathbf{F}_j^{(g)\alpha}) \right], \tag{28}$$

where $\mathbf{A}^\alpha = \Sigma_{i=1}^{N_\alpha} \mathbf{A}_i^{(h)\alpha}$ Combining Eqs. (11) and (28), the translational equation of motion for spheroid i is

$$\dot{\mathbf{r}}_i^\alpha = \sum_{j=1}^{N_\alpha} \boldsymbol{\omega}_j^\alpha \times \mathbf{b}_{ji}^\alpha - (\mathbf{A}^\alpha)^{-1} \cdot \left[\sum_{j=1}^{N_\alpha} \sum_{k=1}^{N_\alpha} \mathbf{A}_j^{(h)\alpha} \cdot (\boldsymbol{\omega}_k^\alpha \times \mathbf{b}_{kj}^\alpha) - \sum_{j=1}^{N_\alpha} (\mathbf{A}_j^{(h)\alpha} \cdot \mathbf{U}_j^{(\infty)\alpha} + \mathbf{F}_j^{(p)\alpha} + \mathbf{F}_j^{(g)\alpha}) \right]. \tag{29}$$

To evaluate the rotational equations of motion, we first solve Eq. (26) for the constraint forces by rewriting the N_α equations as a matrix equation and then multiplying this equation by $\underline{T}^\alpha$. Next, the hydrodynamic torque [Eq. (18)] and constraint forces, with the hydrodynamic force written in terms of Eq. (11), are substituted into Eq. (27). Solving the resulting equation for the angular velocities, the rotational equation of motion for spheroid i is

$$\sum_{l=1}^{N_\alpha} \mathbf{Q}_{il}^\alpha \cdot \boldsymbol{\omega}_l^\alpha = \mathbf{D}_i^\alpha, \tag{30}$$

where

$$\mathbf{Q}_{il}^\alpha = \delta_{il} \mathbf{C}_i^{(h)\alpha} - \sum_{j=1}^{N_\alpha} \tilde{\mathbf{d}}_{ij}^\alpha \cdot \mathbf{A}_j^{(h)\alpha} \cdot \tilde{\mathbf{b}}_{lj}^\alpha + \sum_{j=1}^{N_\alpha} \sum_{k=1}^{N_\alpha} \tilde{\mathbf{d}}_{ij}^\alpha \cdot \mathbf{A}_j^{(h)\alpha} \cdot (\mathbf{A}^\alpha)^{-1} \cdot \mathbf{A}_k^{(h)\alpha} \cdot \tilde{\mathbf{b}}_{lk}^\alpha,$$

$$\mathbf{D}_i^\alpha = \mathbf{M}_i^{(p)\alpha} - \sum_{j=1}^{N_\alpha} \mathbf{d}_{ij}^\alpha \times \left[\mathbf{A}_j^{(h)\alpha} \cdot \mathbf{U}_j^{(\infty)\alpha} + \mathbf{F}_j^{(p)\alpha} + \mathbf{F}_j^{(g)\alpha} - \mathbf{A}_j^{(h)\alpha} \cdot (\mathbf{A}^\alpha)^{-1} \cdot \sum_{k=1}^{N_\alpha} (\mathbf{A}_k^{(h)\alpha} \cdot \mathbf{U}_k^{(\infty)\alpha} + \mathbf{F}_k^{(p)\alpha} + \mathbf{F}_k^{(g)\alpha}) \right] + \mathbf{C}_i^{(h)\alpha} \cdot \boldsymbol{\Omega}^{(\infty)} + \tilde{\mathbf{H}}_i^{(h)\alpha} : \mathbf{E}^{(\infty)} + \sum_{j=1}^{N_\alpha} S_{ij}^\alpha \mathbf{Y}_j^\alpha,$$

$$\tilde{\mathbf{d}}_{ij}^\alpha = \begin{bmatrix} 0 & -d^\alpha_{z_{ij}} & d^\alpha_{y_{ij}} \\ d^\alpha_{z_{ij}} & 0 & -d^\alpha_{x_{ij}} \\ -d^\alpha_{y_{ij}} & d^\alpha_{x_{ij}} & 0 \end{bmatrix},$$

$$\tilde{\mathbf{b}}_{lj}^\alpha = \begin{bmatrix} 0 & -b^\alpha_{z_{lj}} & b^\alpha_{y_{ij}} \\ b^\alpha_{z_{ij}} & 0 & -b^\alpha_{x_{ij}} \\ -b^\alpha_{y_{ij}} & b^\alpha_{x_{ij}} & 0 \end{bmatrix}.$$

To solve Eq. (30) for the angular velocities $\boldsymbol{\omega}_l^\alpha$, the tensor components of $\mathbf{Q}_{il}^\alpha$ $(i,l=1,\ldots,N_\alpha)$ are combined into a $3N_\alpha \times 3N_\alpha$ scalar matrix and inverted. The time de-

rivatives of the Euler parameters can be computed from the relative angular velocities $\mathbf{\Omega}_i^\alpha$,

$$\begin{bmatrix} \dot{q}_{1i}^\alpha \\ \dot{q}_{2i}^\alpha \\ \dot{q}_{3i}^\alpha \\ \dot{q}_{4i}^\alpha \end{bmatrix} = \frac{1}{2} \begin{bmatrix} 0 & -\Omega_{x_i}^\alpha & -\Omega_{y_i}^\alpha & -\Omega_{z_i}^\alpha \\ \Omega_{x_i}^\alpha & 0 & \Omega_{z_i}^\alpha & -\Omega_{y_i}^\alpha \\ \Omega_{y_i}^\alpha & -\Omega_{z_i}^\alpha & 0 & \Omega_{x_i}^\alpha \\ \Omega_{z_i}^\alpha & \Omega_{y_i}^\alpha & -\Omega_{x_i}^\alpha & 0 \end{bmatrix} \begin{bmatrix} q_{1i}^\alpha \\ q_{2i}^\alpha \\ q_{3i}^\alpha \\ q_{4i}^\alpha \end{bmatrix}, \quad (31)$$

where the relative angular velocities are determined from Eq. (12). These relative angular velocities must first be transformed into their respective body-fixed frames of reference.

From Eqs. (29) and (31), the dynamical behavior of each fiber in the suspension can be determined. To limit the number of fibers simulated, periodic boundary conditions are applied. With these boundary conditions it is possible to simulate a suspension of infinite extent by only following the motion of a small number of fibers in a simulation box. A discussion of periodic boundary conditions can be found in Ref. 23. The Euler parameters should be periodically normalized during simulation via

$$q_{ik}^\alpha = q_{ik}^\alpha \left[\sum_{j=1}^{4} (q_{jk}^\alpha)^2 \right]^{-1/2}, \quad i=1,\ldots,4, \quad (32)$$

because of computer round-off error.

Simulating fiber dynamics with chains composed of spheroids rather than spheres can dramatically decrease computation time. For example, for isolated rigid fibers with an overall aspect ratio of $a_r=100$, the cpu time per time step for fibers composed of 10 spheroids ($a/b=10$) is 260 times smaller than when the fiber is composed of 100 spheres. In this case, the computation time is dominated by solving Eq. (30) for the angular velocities, which is, of course, faster for smaller N_α. In simulations of suspensions containing many interacting fibers, the majority of the computation time is spent evaluating interactions between spheroids in different chains, as opposed to solving Eq. (30)—thus the computation time will again be smaller when spheroids are employed instead of spheres. For a suspension of 102 fibers of aspect ratio $a_r=25$, the cpu time per time step when the fibers are composed of 5 spheroids ($a/b=5$) is 22.7 times smaller than when the fibers are composed of 20 spheroids of aspect ratio $a/b=1.25$.

III. SINGLE FIBER DYNAMICS

To test the simulation method, the motion of an isolated, neutrally buoyant fiber in an unbounded simple shear flow was analyzed. Equal bending constants, k_B^α, were used in each joint and there were no intraparticle interactions (spheroid overlap is avoided by using sufficiently large k_B^α). The fiber was initially straight and aligned along the y axis with the center of mass located at the fixed reference frame origin. Twisting constants, k_T^α, do not need to be specified because with this initial configuration, the fiber does not rotate out of the x-y plane and no torques act to twist the fiber. The bulk rate of strain tensor and vorticity for simple shear flow are given in Cartesian components as

$$\mathbf{E}^{(\infty)} = \frac{\dot{\gamma}}{2} \begin{bmatrix} 0 & 1 & 0 \\ 1 & 0 & 0 \\ 0 & 0 & 0 \end{bmatrix}$$

and

$$\mathbf{\Omega}^{(\infty)} = -\frac{\dot{\gamma}}{2}[0 \quad 0 \quad 1], \quad (33)$$

where $\dot{\gamma}$ is the shear rate in the x-y plane.

To nondimensionalize the equations of motion, the length, time and force scales are selected as $2b$, $\pi\eta b^3/k_B^\alpha$, and k_B^α/b, respectively. The resistance tensor $\mathbf{A}_i^{(h)\alpha}$, relating force to translational velocity is made dimensionless by $6\pi\eta a$, and the tensors $\mathbf{C}_i^{(h)\alpha}$ and $\tilde{\mathbf{H}}_i^{(h)\alpha}$, relating torque to angular velocity and rate of strain, respectively, by $8\pi\eta a^3$. With this scaling, the dimensionless shear rate $\dot{\gamma}^*$ is the ratio of hydrodynamic forces to bending resistance,

$$\dot{\gamma}^* = \frac{\pi\eta b^3 \dot{\gamma}}{k_B^\alpha}. \quad (34)$$

The translational equation of motion for spheroid i in dimensionless form is

$$\dot{\mathbf{r}}_i^{\alpha *} = \sum_{j=1}^{N_\alpha} \boldsymbol{\omega}_j^{\alpha *} \times \mathbf{b}_{ji}^{\alpha *} - 3\left(\frac{b}{a}\right)^2 (\mathbf{A}^{\alpha *})^{-1} \cdot \left[\sum_{j=1}^{N_\alpha} \sum_{k=1}^{N_\alpha} \mathbf{A}_j^{(h)\alpha *} \cdot (\boldsymbol{\omega}_k^{\alpha *} \times \mathbf{b}_{kj}^{\alpha *}) - \sum_{j=1}^{N_\alpha} (\mathbf{A}_j^{(h)\alpha *} \cdot \dot{\gamma}^* y_j^{\alpha *} \mathbf{e}_x + \mathbf{F}_j^{(p)\alpha *}) \right], \quad (35)$$

where the asterisks signify dimensionless quantities, and $y_j^{\alpha *}$ is the y^*-coordinate position of spheroid j in fiber α. The rotational equation of motion for spheroid i in dimensionless form is

$$\sum_{l=1}^{N_\alpha} \mathbf{Q}_{il}^{\alpha *} \cdot \boldsymbol{\omega}_l^{\alpha *} = \mathbf{D}_i^{\alpha *}, \quad (36)$$

where

$$\mathbf{Q}_{il}^{\alpha *} = \delta_{il} \mathbf{C}_i^{(h)\alpha *} - 3\left(\frac{b}{a}\right)^2 \left[\sum_{j=1}^{N_\alpha} \tilde{\mathbf{d}}_{ij}^{\alpha *} \cdot \mathbf{A}_j^{(h)\alpha *} \cdot \tilde{\mathbf{b}}_{lj}^{\alpha *} - \sum_{j=1}^{N_\alpha} \sum_{k=1}^{N_\alpha} \tilde{\mathbf{d}}_{ij}^{\alpha *} \cdot \mathbf{A}_{jk}^{(2)\alpha *} \cdot \tilde{\mathbf{b}}_{lk}^{\alpha *} \right],$$

and

$$\mathbf{D}_i^{\alpha*} = \frac{1}{4}\left(\frac{b}{a}\right)^3 \mathbf{M}_i^{(p)\alpha*} - \left(\frac{b}{a}\right)^2 \sum_{j=1}^{N_\alpha} \mathbf{d}_{ij}^{\alpha*} \times \left[3\mathbf{A}_j^{(h)\alpha*} \cdot \dot{\gamma}^* y_j^{\alpha*} \mathbf{e}_x + \frac{1}{4}\left(\frac{b}{a}\right) \mathbf{F}_j^{(p)\alpha*} \right.$$
$$\left. - \mathbf{A}_j^{(1)\alpha*} \cdot \sum_{k=1}^{N_\alpha} \left(3\mathbf{A}_k^{(h)\alpha*} \cdot \dot{\gamma}^* y_k^{\alpha*} \mathbf{e}_x + \frac{1}{4}\left(\frac{b}{a}\right) \mathbf{F}_k^{(p)\alpha*} \right) \right] - \mathbf{C}_i^{(h)\alpha*} \cdot \frac{1}{2}\dot{\gamma}^* \mathbf{e}_z$$
$$+ \tilde{\mathbf{H}}_i^{(h)\alpha*} : \frac{1}{2}\dot{\gamma}^* (\mathbf{e}_x \mathbf{e}_y + \mathbf{e}_y \mathbf{e}_x) + \frac{1}{4}\left(\frac{b}{a}\right)^3 \sum_{j=1}^{N_\alpha} S_{ij}^\alpha \mathbf{Y}_j^{\alpha*} .$$

The internal hinge torque, $\mathbf{Y}_j^{\alpha*}$, in general, in dimensionless form is

$$\mathbf{Y}_j^{\alpha*} = -\frac{1}{2}\left[(\theta_j^\alpha - \theta^{(0)\alpha})\mathbf{n}_{pb} + k_T^{\alpha*}(\phi_j^\alpha - \phi^{(0)\alpha}) \times \frac{\mathbf{c}_{i^{(-)}\alpha(j)j}^\alpha}{\|\mathbf{c}_{i^{(-)}\alpha(j)j}^\alpha\|} \right], \tag{37}$$

where $k_T^{\alpha*} = k_T^\alpha / k_B^\alpha$ (the second term is zero for simulations in the plane of shear). The equilibrium angles $\theta^{(0)\alpha}$ and $\phi^{(0)\alpha}$ are equal to π and 0, respectively, for a nominally straight fiber. From the dimensionless form of the equations of motion, the dynamic behavior of a isolated fiber in an unbounded simple shear flow, oriented in the x-y plane, is characterized by the dimensionless shear rate $\dot{\gamma}^*$ and the fiber aspect ratio $a_r \equiv a N_\alpha / b$.

The effect of the dimensionless shear rate, $\dot{\gamma}^*$, on the rotational motions of a model fiber are illustrated in Fig. 7 for a fiber composed of 20 spheroids each with an aspect ratio of 1.25 ($a_r = 25$). At $\dot{\gamma}^* = 2.56 \times 10^{-3}$ [Fig. 7(a)], the fiber is extremely flexible and deforms into an S-shape during its rotational orbit. Forgacs and Mason[3,4] observed this motion experimentally for rayon fibers suspended in corn syrup and have termed the orbit an ''S-turn.'' For a smaller shear rate of $\dot{\gamma}^* = 6.4 \times 10^{-4}$ [Fig. 7(b)], the deformation is no longer symmetric about the center of mass and one end of the fiber loops over to complete a rotation. This motion has also been observed by Forgacs and Mason and is called a ''snake turn.'' Note that in Figs. 7(a) and 7(b), the deformed fiber shapes are not symmetric with respect to 180° rotation about the z axis. Such deformations in fibers, observed experimentally, have been associated with buckling instabilities.[3,24] Finally, when the shear rate is reduced to $\dot{\gamma}^* = 1.28 \times 10^{-4}$ [Fig. 7(c)], the fiber model barely bends (the end-to-end distance deviates $< 0.1\%$ during an orbit) and undergoes a periodic rotational orbit about its center of mass similar to that of a rigid fiber, spending most of its time in the flow direction.

The simulated periods of rotation T_J (scaled by $\dot{\gamma}$) for rigid fibers are plotted as a function of aspect ratio in Fig. 8 ($\dot{\gamma}^*$ was adjusted in each simulation to ensure that the end-to-end distance deviated $< 0.1\%$ during an orbit). In the simulations, two different fiber models were used. In one model, the fiber was composed of 10 prolate spheroids and the spheroid aspect ratio (a/b) was adjusted to set the fiber aspect ratio ($a_r = a10/b$). In the other model, each spheroid had an aspect ratio of 1 (a sphere), and thus the fiber aspect

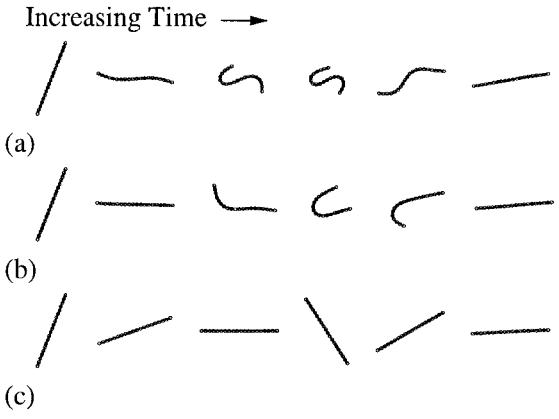

FIG. 7. Snapshots of fiber configurations during simple, unbounded shear flow. The fibers are in the plane of shear, and the snapshots are at times increasing from left to right. (a) $\dot{\gamma}^* = \pi \eta b^3 \dot{\gamma} / k_B^\alpha = 2.56 \times 10^{-3}$, (b) $\dot{\gamma}^* = 6.4 \times 10^{-4}$, and (c) $\dot{\gamma}^* = 1.28 \times 10^{-4}$.

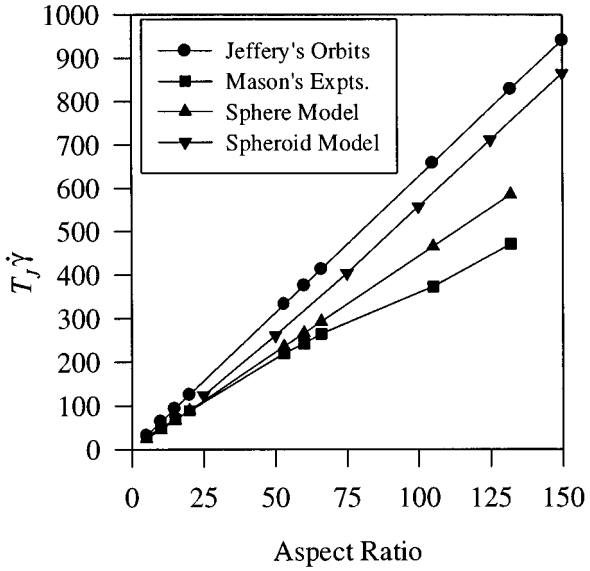

FIG. 8. Comparison of simulated, theoretical, and experimentally measured periods of rotation for rigid fibers as a function aspect ratio in simple shear flow.

TABLE II. Comparison of fiber model and equivalent ellipsoid aspect ratios.

Sphere model		Spheroid model	
Fiber aspect ratio	Equivalent aspect ratio	Fiber aspect ratio	Equivalent aspect ratio
a_r	a_{r_e}	a_r	a_{r_e}
5	3.61	25	19.7
10	7.11	50	41.7
20	14.2	75	64.3
53	37.5	100	88.4
66	46.6	125	113.4
105	74.3	150	137.9
132	93.4		

ratio equals N_α. As the spheroid aspect ratio approaches one, the periods of the two fiber models become equivalent, as expected. Also plotted in Fig. 8 are the theoretical periods for single, rigid prolate spheroids derived by Jeffery,[2] as well as the experimental results for rigid cylinders reported by Goldsmith and Mason.[24] The differences between these two data sets illustrate that for rigid bodies of fixed aspect ratio (large dimension/small dimension), the period still depends upon the shape of the body. The simulation results, although not exact since hydrodynamic interactions are neglected (implications of neglecting hydrodynamic interactions are discussed further below), agree qualitatively with the established trends—the period increases with aspect ratio and depends on the fiber shape.

The motion of any rigid, axisymmetric ''fiber'' is described by Jeffrey's analysis for rigid prolate spheroids,[2] when the appropriate equivalent fiber aspect ratio is inserted into the dynamical equations; this equivalent aspect ratio is simply the aspect ratio of a prolate spheroid that gives the same period of rotation as the rigid fiber.[24] The equivalent aspect ratios for the spheroid and sphere models are presented in Table II. We find that the simulated rigid fiber motion, in both two and three dimensions, agrees with Jeffery's theory in all aspects examined. For example: performing simulations over 20 revolutions, we observe no drift in the orbit constant; the period of rotation is independent of orbit constant; and the spinning rate about the fiber axis agrees quantitatively with predictions. Comparisons of rigid and flexible fiber motions with a variety of existing theoretical and experimental results will appear in a future publication.[25]

The prevalent features of dynamics of isolated fibers are thus qualitatively reproduced by the linked-rigid-body model for both flexible and rigid fibers. In the next section, we examine the behavior of suspensions of these fibers, focusing on the rheological properties.

IV. SIMULATION OF A SHEARED SUSPENSION

In this section, the simulation method is used to examine the transient rheology of a suspension of N_f neutrally buoyant fibers in simple shear flow. Each fiber has the same aspect ratio and uniform bending and twisting constants in each joint. The fibers interact only through a short-range repulsive force which prevents overlap of the spheroids. Other types of interparticle forces will be considered in future publications.

The short-range repulsive force between two spheroids is modeled by the function

$$\mathbf{F}_{ij}^{(r)*} = -F_0^* e^{-\kappa^* h_{ij}^*} \mathbf{e}_{h_{ij}}, \tag{38}$$

where $\mathbf{F}_{ij}^{(r)*}$ is the force on spheroid i due to spheroid j, h_{ij}^* is the minimum separation between the surfaces of the two spheroids, κ^* is the range on the repulsive force, F_0^* is a constant, and $\mathbf{e}_{h_{ij}^*}$ is a unit vector along the line of minimum separation directed from spheroid i to j. The minimum separation is calculated using an algorithm described by Claeys and Brady.[10] Because the repulsive force is directed along the line of minimum separation, which does not necessarily pass through the centroid, it can produce an interparticle torque,

$$\mathbf{M}_{ij}^{(r)*} = (\mathbf{z}_i^{\alpha*} - \mathbf{r}_i^{\alpha*}) \times \mathbf{F}_{ij}^{(r)*} = -\mathbf{M}_{ji}^{(r)*}, \tag{39}$$

where $\mathbf{M}_{ij}^{(r)*}$ is the torque on spheroid i due to spheroid j, and $\mathbf{z}_i^{\alpha*}$ is the point where the line of minimum separation intersects the surface of spheroid i in fiber α. The total interparticle force $\mathbf{F}_i^{(p)\alpha*}$ and torque $\mathbf{M}_i^{(p)\alpha*}$ are the summations over all pair interactions with spheroid i.

The dimensionless dynamical equations for each fiber in the suspension are given in Eqs. (35) and (36). From these equations, there are six dimensionless parameters which characterize suspension flow behavior: the volume fraction of fibers $\phi \equiv 4\pi a b^2 N_f N_\alpha / 3L^3$, where L is the length of one side of the cubic simulation box; the fiber aspect ratio a_r; the range of the repulsive force, $1/\kappa^*$; the repulsive force constant F_0^*; the torsional spring constant $k_T^{\alpha*}$ and the shear rate $\dot{\gamma}^*$, which is the ratio of hydrodynamic forces to bending resistance in the fiber.

A. Rheology of fiber suspensions

For a statistically homogeneous suspension of particles (spheroids), the bulk stress $\boldsymbol{\Sigma}$ can be defined as[26]

$$\boldsymbol{\Sigma} = \frac{1}{V} \int_V \boldsymbol{\sigma} dV, \tag{40}$$

where $\boldsymbol{\sigma}$ is the local stress in the suspending medium and V is a statistically suitable volume of the suspension. Taking the suspending fluid to be Newtonian, Eq. (40) can be written as

$$\boldsymbol{\Sigma} = -p\boldsymbol{\delta} + 2\eta \mathbf{E}^{(\infty)} + \frac{1}{V} \sum_i \int_{V_0} \boldsymbol{\sigma} dV, \tag{41}$$

where p is the pressure, η is the viscosity of the suspending fluid, V_0 is the particle volume, and the summation is over all particles. The first term represents the isotropic contribution of no interest for incompressible suspensions, the second term is the deviatoric stress that would exist in the absence of the particles, and the third term is the contribution to the bulk stress arising from the presence of the particles.

For non-Brownian particles, Batchelor[26,27] has shown that the particle stress contribution may be formulated as

$$\frac{1}{V}\sum_i \int_{V_o} \boldsymbol{\sigma} dV = n\left(\langle \mathbf{S}^{(h)} \rangle - \langle \mathbf{r}\mathbf{F}^{(p)} \rangle + \frac{1}{2}\langle \boldsymbol{\epsilon}\cdot\mathbf{L} \rangle \right), \tag{42}$$

where n is the number density of particles and the angular brackets indicate a volume average. The quantity $\mathbf{S}^{(h)}$ is the hydrodynamic stresslet and physically represents the added mechanical or contact stresses due to the resistance of the rigid particles to the local deformation of the fluid.[28] In the absence of hydrodynamic interactions and fluid inertia, the stresslet on a prolate spheroid can be written in terms of the resistance tensors $\mathbf{H}_i^{(h)\alpha}$ and $\mathbf{M}_i^{(h)\alpha}$ as[22]

$$n\langle \mathbf{S}^{(h)} \rangle = \frac{1}{V}\sum_{\alpha=1}^{N_f}\sum_{i=1}^{N_\alpha} [\mathbf{H}_i^{(h)\alpha}\cdot(\boldsymbol{\Omega}^{(\infty)} - \boldsymbol{\omega}_i^\alpha) + \mathbf{M}_i^{(h)\alpha} : \mathbf{E}^{(\infty)}]. \tag{43}$$

These resistance tensors depend only on the instantaneous orientation of spheroid i. The quantity $-n\langle \mathbf{r}\mathbf{F}^{(p)} \rangle$ is the elastic or thermodynamic stress,

$$n\langle \mathbf{r}\mathbf{F}^{(p)} \rangle = \frac{1}{V}\sum_{\alpha=1}^{N_f}\sum_{i=1}^{N_\alpha} \mathbf{r}_i^\alpha \mathbf{F}_i^{(p)\alpha}. \tag{44}$$

Note that the constraint forces are not included in Eq. (44) because ideal forces do no work in virtual displacements. The remaining term $\frac{1}{2}\langle \boldsymbol{\epsilon}\cdot\mathbf{L} \rangle$ comes from an angular momentum balance on the particles and adds the effect of any nonhydrodynamic torques, $\mathbf{L}_i^\alpha$ acting on the particles,

$$n\frac{1}{2}\langle \boldsymbol{\epsilon}\cdot\mathbf{L} \rangle = \frac{1}{2V}\sum_{\alpha=1}^{N_f}\sum_{i=1}^{N_\alpha} \boldsymbol{\epsilon}\cdot[\mathbf{M}_i^{(p)\alpha} - \sum_{j=1}^{N_\alpha} [\mathbf{d}_{ij}^\alpha \times (\mathbf{F}_j^{(h)\alpha} + \mathbf{F}_j^{(p)\alpha}) - S_{ij}^\alpha \mathbf{Y}_j^\alpha]], \tag{45}$$

where $\boldsymbol{\epsilon}$ is the permutation tensor. Here, the constraint forces are included because they do contribute to the angular momentum balance.

The relative viscosity, η_r, is defined as the suspension shear viscosity divided by the viscosity of the suspending fluid,

$$\eta_r = 1.0 + \eta^H + \eta^{rF} + \eta^L, \tag{46}$$

where, in dimensionless form,

$$\eta^H = \left(\frac{a}{b}\right)^2 \phi \frac{1}{\dot{\gamma}^* N}\sum_{\alpha=1}^{N_f}\sum_{i=1}^{N_\alpha} [6\mathbf{H}_i^{(h)\alpha *}\cdot(\boldsymbol{\Omega}^{(\infty)*} - \boldsymbol{\omega}_i^{\alpha *}) + \mathbf{M}_i^{(h)\alpha *} : \mathbf{E}^{(\infty)*}]_{yx},$$

$$\eta^{rF} = -\frac{3}{2}\left(\frac{a}{b}\right)^{-1} \phi \frac{1}{\dot{\gamma}^* N}\sum_{\alpha=1}^{N_f}\sum_{i=1}^{N_\alpha} [\mathbf{r}_i^{\alpha *}\mathbf{F}_i^{(p)\alpha *}]_{yx},$$

$$\eta^L = -\frac{3}{2}\left(\frac{a}{b}\right)^{-1} \phi \frac{1}{\dot{\gamma}^* N}\sum_{\alpha=1}^{N_f}\sum_{i=1}^{N_\alpha} \left[\mathbf{M}_i^{(p)\alpha *} - \sum_{j=1}^{N_\alpha} \left[\mathbf{d}_{ij}^{\alpha *} \times \left(12\left(\frac{a}{b}\right)\mathbf{F}_j^{(h)\alpha *} + \mathbf{F}_j^{(p)\alpha *} \right) - S_{ij}^\alpha \mathbf{Y}_j^{\alpha *} \right] \right]_{yx},$$

and $N = N_f N_\alpha$. η^H, η^{rF}, and η^L are the dimensionless hydrodynamic, interparticle, and external torque contributions to the relative viscosity, respectively.

B. Dynamic simulation results: Relative viscosity

Simulations were performed to investigate the transient behavior of the suspension relative to viscosity under simple shear flow. To generate the initial suspension configuration, N_{fp} straight fibers were randomly placed on N_p y^*-z^* planes distributed evenly along the x^* axis, where $N_p = N_f / N_{fp}$. N_{fp} was chosen so that the N_f fibers would fit in the N_p planes in the periodic simulation box of volume $(1.5a_r)^3$ without fiber overlap. The fibers were then displaced and rotated randomly to disrupt the order in the suspension microstructure. All simulations reported here employed 102 fibers, composed of 5 spheroids with an aspect ratio of 5 ($a_r = 25$), corresponding to a fiber volume fraction of 0.0255. The repulsive force parameter $\kappa^* = 100$, the force constant $F_0^* = 1$, and $k_T^{\alpha *} = 0.01$.

The relative viscosity for a suspension of relatively rigid fibers ($\dot{\gamma}^* = 2.0 \times 10^{-4}$) is presented in Fig. 9(a), where time is scaled by the period, T_J, of a rigid fiber Jeffery orbit. The viscosity oscillates with time, but the oscillations appear to decay, with the viscosity approaching a constant at long times. There is apparently no significant drift in the time-averaged viscosity at long times; longer simulations would need to be performed to verify this. The period is roughly one-half of the rotational period of an isolated rigid fiber. The maxima correspond to an average fiber orientation at angles of 45° and 135° from the x^* axis. The minima result from an average fiber orientation along the x^* axis. The particle contributions in Fig. 9(b) illustrate that the viscosity is dominated by the hydrodynamic contribution, and that the oscillations result from the changes in the spheroid hydrodynamic stresslet as the fiber rotates. The interparticle forces and nonhydrodynamic torques only make a small contribution. Ivanov *et al.*[29] observed a similar oscillatory response with nylon fibers in Castor Oil. The decay of the oscillations was shown to be mainly due to particle interactions. In the simulations, the interactions appear to make the orientation distribution more uniform.

The transient response for a suspension of more flexible fibers ($\dot{\gamma}^* = 2 \times 10^{-2}$) is presented in Fig. 10. Again, the oscillation in viscosity decays, with no significant drift in the time-averaged viscosity at long times, within the finite time simulated. The period of oscillation is smaller than observed for rigid fibers which can be attributed to a reduction in the end-to-end distance of the fibers due to bending. Forgacs and Mason[4] observed similar changes in the rotational period when fibers would undergo the snake turn discussed above. Comparison of the steady-state viscosities given in Figs. 9 and 10 indicates that flexibility has little effect on the magnitude of the suspension viscosity, under the conditions simulated. Fiber flexibility does increase the hydrodynamic contribution to the viscosity, but reduces the nonhydrodynamic torque contribution.

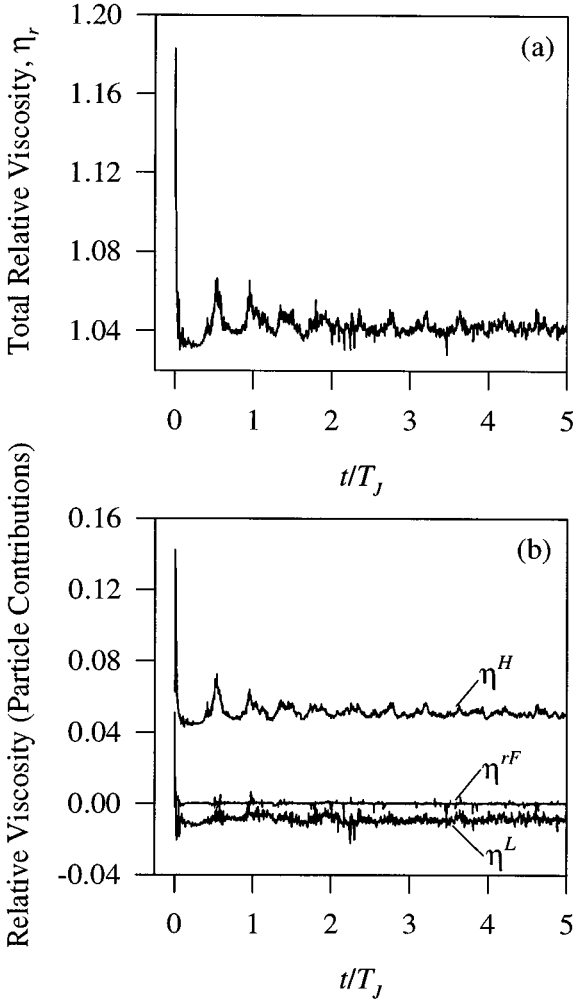

FIG. 9. Transient behavior in the (a) suspension relative viscosity and (b) particle contributions at $\phi=0.0255$ for rigid fibers ($\dot{\gamma}^*=2.0\times10^{-4}$) with an aspect ratio of 25.

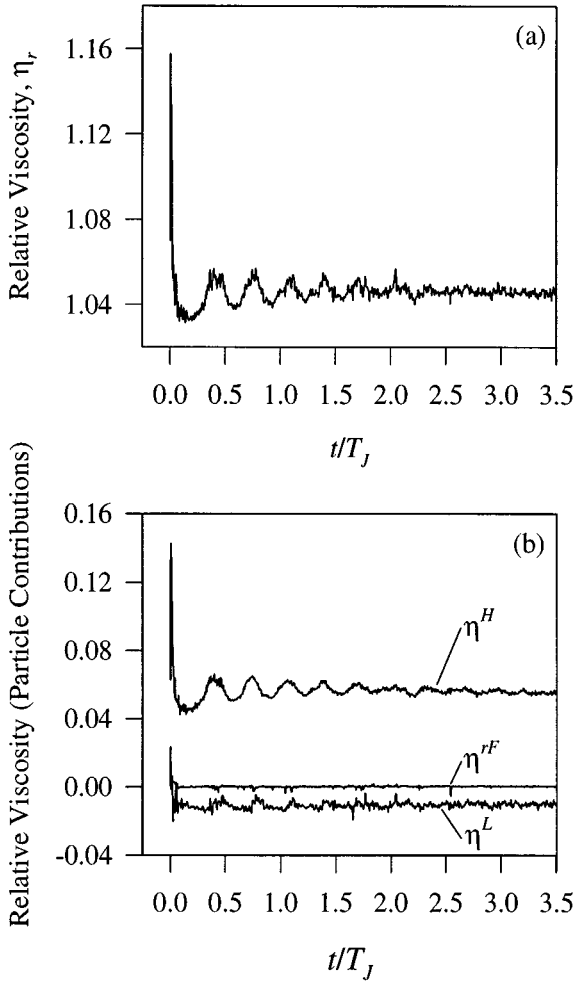

FIG. 10. Transient behavior in the (a) suspension relative viscosity and (b) particle contributions at $\phi=0.0255$ for flexible fibers ($\dot{\gamma}^*=2.0\times10^{-2}$) with an aspect ratio of 25.

Simulated viscosities can be compared with experimental and theoretical results. Simulations of rigid fibers with an aspect ratio of 25 at $\phi=0.0255$ produce a steady-state relative viscosity of $\eta_r=1.04$ (Fig. 9). Interpolating from the experimental data of Ganani and Powell[30] for glass fibers with an aspect ratio 24.3, one obtains a relative viscosity of about 1.1, similar to the simulated value. From a diagrammatic theory for high aspect ratio fibers, Shaqfeh and Fredrickson,[31] derived an expression for the relative viscosity for random orientations of slender ellipsoids,

$$\eta_r-1=\frac{\pi nL^3}{3\ln(1/\phi)}\left\{1-\frac{\ln\ln(1/\phi)}{\ln(1/\phi)}-\frac{0.6170}{\ln(1/\phi)}\right\}, \qquad (47)$$

where n is fiber number density and L is the fiber length. The relative viscosity calculated from Eq. (47) is 2.0. The discrepancy between this value and our simulated result can be attributed to at least three differences between the theory and the simulations. First, the theory was derived in the limit of large fiber aspect ratios. Second, hydrodynamic interactions are neglected in the simulations. Third, the theory assumes an isotropic suspension structure. However, the simulations give reasonable values and reproduce observed transient behavior in the relative viscosity under simple shear flow.

We close this section with a few comments about the impact of neglecting hydrodynamic interactions. These were neglected in this preliminary study in order to reduce computation time. Including hydrodynamic as well as other types of interactions will clearly influence the magnitudes of calculated properties, particularly the suspension viscosity. We note, however, that certain features, such as the Jeffery orbits, flexible fiber motions, and the transient rheological properties, are qualitatively reproduced without including hydrodynamic interactions, suggesting that much of the essential physics is incorporated in the model. Finally, many real fibers (e.g., wood pulp fibers) are often rough, porous, and interact through a variety of forces, including friction and colloidal forces. It is apparent that hydrodynamic interactions between rigid bodies are but one type of interaction that must be included in order to quantitatively reproduce many experimental observations. This is the subject of future work.

V. CONCLUSIONS

In this paper, a particle-level simulation method was employed to study the dynamics of flowing suspensions of rigid and flexible fibers. Fibers were modeled as chains of prolate spheroids connected through ball and socket joints. The three degrees of rotational freedom in the joints enable the model to bend and twist. By varying the resistance in the joints both flexible and rigid fibers were modeled. Repulsive interactions between fibers were also included, but hydrodynamic interactions and particle inertia were neglected in this implementation. The motion of each fiber was determined by solving the translational and rotational equations of motion for each spheroid.

Simulations of isolated fibers in shear flow demonstrated that the method can reproduce known dynamical behavior of both rigid and flexible fibers in a flow field. For rigid fibers, the periods of rotation agreed with those from Jeffery's calculations and the flexible fiber motions were similar to the experimental observations of Forgacs and Mason.

The simulation method was also used to investigate the transient behavior in the suspension relative viscosity under simple shear flow. At a volume fraction of $\phi = 0.0255$, for rigid fibers with an aspect ratio of 25, the simulations gave an oscillatory response that decayed to a steady-state. This agrees with the experimental observations of Ivanov *et al.* Comparison of calculated steady-state viscosities with experimental and theory showed good agreement. An increase in fiber flexibility reduced the period in the transient oscillations; however, this had little effect on the magnitude of the steady-state viscosities. Fiber flexibility does increase the hydrodynamic contribution to the viscosity, but decreases the nonhydrodynamic torque contribution. Future publications will explore the effect of concentration, aspect ratio, flexibility, shear rate, and interparticle interactions on the microstructure and rheology of fiber suspensions.

These results verify that rigid and flexible fibers can indeed be modeled with linked rigid bodies, where the rigid bodies themselves can be elongated (e.g., prolate spheroids). Modeling fibers with fewer elongated bodies, as opposed to many spheres, significantly reduces computation time and facilitates the study of suspensions of many interacting, long fibers.

ACKNOWLEDGMENTS

This work was supported in part by a grant from the Tappi Foundation, and the National Science Foundation (Grant No. CTS-9502276). Appreciation is also extended to R. A. Halcomb for his helpful suggestions in this work.

[1] J. S. Cintra and C. L. Tucker, J. Rheol. **39**, 1095 (1995).
[2] G. B. Jeffery, Proc. R. Soc. London, Ser. A **102**, 161 (1922).
[3] O. L. Forgacs and S. G. Mason, J. Colloid Interface Sci. **14**, 457 (1959).
[4] O. L. Forgacs and S. G. Mason, J. Colloid Interface Sci. **14**, 473 (1959).
[5] G. K. Batchelor, J. Fluid Mech. **46**, 813 (1971).
[6] S. M. Dinh and R. C. Armstrong, J. Rheol. **28**, 207 (1984).
[7] S. Toll and J. E. Månson, J. Rheol. **38**, 985 (1994).
[8] M. Rahnama, D. L. Koch, and E. S. G. Shaqfeh, Phys. Fluids **7**, 487 (1995).
[9] F. Folgar and C. L. Tucker, J. Reinf. Plastics Compos. **3**, 98 (1984).
[10] I. L. Claeys and J. F. Brady, J. Fluid Mech. **251**, 411 (1993).
[11] I. L. Claeys and J. F. Brady, J. Fluid Mech. **251**, 443 (1993).
[12] I. L. Claeys and J. F. Brady, J. Fluid Mech. **251**, 479 (1993).
[13] Y. Yamane, Y. Kaneda, and M. Dio, J. Non-Newtonian Fluid Mech. **54**, 405 (1994).
[14] S. Yamamoto and T. Matsuoka, J. Chem. Phys. **98**, 644 (1993).
[15] S. Yamamoto and T. Matsuoka, J. Chem. Phys. **100**, 3317 (1994).
[16] S. Yamamoto and T. Matsuoka, Poly. Eng. Sci. **35**, 1022 (1995).
[17] S. Yamamoto and T. Matsuoka, J. Chem. Phys. **102**, 2254 (1995).
[18] J. Wittenburg, *Dynamics of Systems of Rigid Bodies* (B. G. Teubner, Stuttgart, 1977).
[19] M. R. Pear and J. H. Weiner, J. Chem. Phys. **71**, 212 (1979).
[20] S. G. Mason, Tappi J. **33**, 440 (1950).
[21] E. J. Haug, *Intermediate Dynamics* (Prentice Hall, Englewood Cliffs, NJ, 1992).
[22] S. Kim and S. J. Karrila, *Microhydrodynamics: Principles and Applications* (Butterworth-Heinemann, Boston, 1991).
[23] M. P. Allen and D. J. Tildesley, *Computer Simulation of Liquids* (Clarendon Press, Oxford, 1987).
[24] H. L. Goldsmith and S. G. Mason, *Rheology*, edited by F. R. Eirich (Academic, New York, 1967), Vol. 4, p. 85.
[25] P. Skjetne, R. F. Ross, and D. J. Klingenberg (unpublished).
[26] G. K. Batchelor, J. Fluid Mech. **41**, 545 (1970).
[27] G. K. Batchelor, J. Fluid Mech. **83**, 97 (1977).
[28] R. T. Bonncaze and J. F. Brady, J. Chem. Phys. **96**, 2183 (1992).
[29] Y. Ivanov, T. G. M. Van De Ven, and S. G. Mason, J. Rheol. **26**, 213 (1982).
[30] E. Ganani and R. L. Powell, J. Comp. Mater. **19**, 194 (1985).
[31] E. S. G. Shaqfeh and G. H. Fredrickson, Phys. Fluids A **2**, 7 (1990).